Results in Physics 78 (2025) 108495

Contents lists available at ScienceDirect

Results in Physics

journal homepage: www.elsevier.com/locate/rinp

Tailoring red and deep-red light: Bi^{3+} doped $Sr_2Gd_{0.2}Eu_{0.8}F_7$ phosphors for next-generation horticultural LEDs

Lj. Đačanin Far *, J. Periša, I. Zeković, Z. Ristić, M. Medić, M.D. Dramićanin, B. Milićević *

Centre of Excellence for Photoconversion, Vinča Institute of Nuclear Sciences-National Institute of the Republic of Serbia, University of Belgrade, P.O. Box 522, 11001 Belgrade, Serbia

ARTICLE INFO

Keywords:
Phosphors
Eu^{3+}
Bi^{3+}
Heavily-doped fluorides
Deep-red emission
LED

ABSTRACT

Eu^{3+}-activated inorganic phosphors are widely used in general lighting and display technologies due to their strong orange/red ($^5D_0 \rightarrow {}^7F_{1,2}$) emissions with wavelengths shorter than 630 nm. However, phosphors activated by Eu^{3+} that strongly emit in the deep-red region, driven by the $^5D_0 \rightarrow {}^7F_4$ transition (>700 nm), are relatively uncommon. This limitation hinders their applicability in horticultural light emitting diodes, where light in the photosynthetically active radiation range, particularly deep-red photons, is crucial for regulating plant growth. Hereby, we prepared Bi^{3+}-doped $Sr_2Gd_{0.2}Eu_{0.8}F_7$ nanoparticles using the hydrothermal synthesis method, to address this challenge. Introducing Bi^{3+} significantly enhanced Eu^{3+} emission under near-UV excitation, with an optimal 1 mol% Bi^{3+} concentration yielding a 250 % increase in integrated emission intensity and a long emission lifetime of 9.3 ms compared to the Bi^{3+}-free sample. The optimized phosphor also demonstrated exceptional thermal stability, retaining 93 % of its room-temperature emission at 200 °C. These results highlight that Bi^{3+}-doping of $Sr_2Gd_{0.2}Eu_{0.8}F_7$ host is a promising strategy for designing thermally robust, deep-red-emitting nanophosphors. Such properties underline their potential for next-generation horticultural LED applications aimed at improving plant growth efficiency.

Introduction

Lanthanide-based phosphors emit electromagnetic radiation across a broad spectral range and are versatile for advanced technologies. They require host matrices that are non-hygroscopic to maintain stability in air and aqueous environments, have low phonon frequencies to minimize non-radiative losses, and possess wide band gaps to facilitate efficient dopant transitions while limiting self-absorption. Fluoride compounds have gained significant attention recently due to their advantageous properties, including low phonon energies (300–500 cm^{-1}), high optical transmittance, and chemical stability. Even though lanthanide (Ln^{3+})-doped alkaline-tetrafluorides with the following formula – $ALnF_4$ (A=Na, K, Li; Ln^{3+}=Y, La, Gd, Lu) – are among the most widely used for efficient luminescence, they exhibit certain limitations in applications that require nanoparticles [1–6]. Recently, the alkali-earth-lanthanide based fluorides (M_2LnF_7, M=Ca, Sr, Ba; Ln^{3+}=Y, La, Gd, Lu) have emerged as advantageous for biomedical imaging, temperature sensing, photothermal treatment and light-emitting diode (LED) applications, exhibiting extremely high up conversion (UC) and down conversion (DC) luminescence, depending on the activator ion [7–14].

Gadolinium-based fluorides are promising phosphor hosts because lanthanide ions can readily substitute Gd^{3+} due to their similar valence and comparable ionic radii. Additionally, Gd^{3+} exhibits a strong absorption peak around 273 nm, which allows it to transfer energy to the activator through nonradiative transitions [15]. Up to now, Sr_2GdF_7 has been mostly used as a host for UC luminescent activators $Yb^{3+}/Er^{3+}/Tm^{3+}/Ho^{3+}$ [13,16–21]. Doping of Sr_2GdF_7 with Eu^{3+} ions was first performed by Runowski *et al.* [22], with concentrations of up to 30 mol %, revealing the intense red emission.

In modern agriculture and food production, there is an increasing focus on developing and implementing efficient LED lighting systems that promote optimal indoor plant growth. The objective is to maximize the conversion of electrical energy into the Photosynthetically Active Radiation (PAR) spectrum, which spans the range of 400 to 700 nm and is essential for driving photosynthesis in plants. Recent studies have demonstrated that deep-red photons (700–750 nm) can work in synergy with higher-energy photons to enhance photochemical efficiency in plants [23–28]. This combination can also improve the flavor quality of crops by mitigating the bitterness often associated with excessive leafy

* Corresponding authors.
E-mail addresses: ljubica.far@vin.bg.ac.rs (Lj. Đačanin Far), bojanam@vin.bg.ac.rs (B. Milićević).

https://doi.org/10.1016/j.rinp.2025.108495
Received 30 July 2025; Received in revised form 3 October 2025; Accepted 17 October 2025
Available online 25 October 2025

Table 1
The exact amounts of precursors needed for the synthesis of 0.0025 mol of $Sr_2Gd_{0.2-x}Eu_{0.8}Bi_xF_7$ (**x** = 0, 0.0025, 0.01, 0.05, 0.10).

Molecular formula	*x*(mol%)	Abbreviated name	Precursor mass (g)					
			$Bi(NO_3)_3$	$Sr(NO_3)_2$	$Eu(NO_3)_3 \cdot 6H_2O$	$Gd(NO_3)_3 \cdot 6H_2O$	NH_4F	EDTA-2Na
$Sr_2Gd_{0.2}Eu_{0.8}F_7$	0	SGEF	–	1.0582	0.8922	0.1947	1.1111	0.9306
$Sr_2Gd_{0.1975}Eu_{0.8}Bi_{0.0025}F_7$	0.25	SGEF_0.25Bi	0.0025			0.1922		
$Sr_2Gd_{0.19}Eu_{0.8}Bi_{0.01}F_7$	1	SGEF_1Bi	0.0099			0.1849		
$Sr_2Gd_{0.15}Eu_{0.8}Bi_{0.05}F_7$	5	SGEF_5Bi	0.0494			0.1460		
$Sr_2Gd_{0.1}Eu_{0.8}Bi_{0.10}F_7$	10	SGEF_10Bi	0.0988			0.0973		

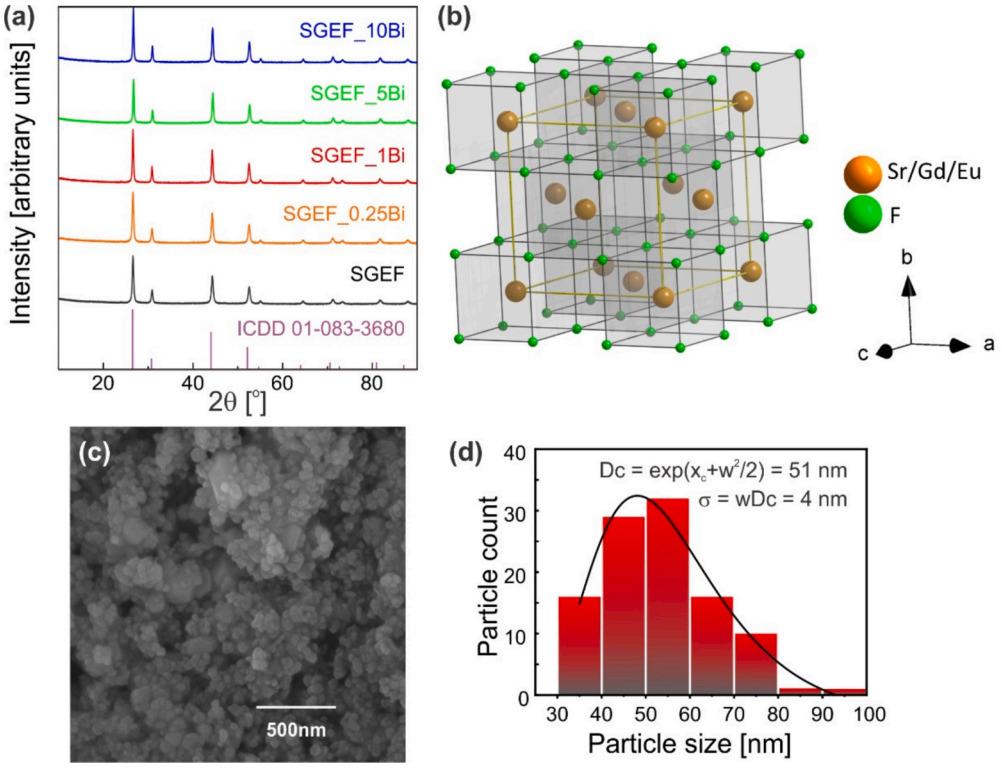

Fig. 1. (a) XRD patterns of the synthesized SGEF_**x** Bi (**x** = 0, 0.25, 1, 5, 10 mol%) nanophosphors; (b) three-dimensional schematic presentation of the $Sr_2Gd_{0.2}Eu_{0.8}F_7$ structure; (c) SEM micrograph and (d) the particle size distribution of the representative SGEF_1Bi nanophosphor, and the formulas for calculating the average particle size.

Table 2
Structural parameters of the SGEF_*x*Bi (x = 0, 0.25, 1, 5, 10 mol%) nanophosphors.

ICDD card 01–083-3680	SGEF	SGEF_0.25Bi	SGEF_1Bi	SGEF_5Bi	SGEF_10Bi
a = b = c (Å)	5.7761 (4)	5.7818(5)	5.7688 (2)	5.7621 (3)	5.7628(3)
CS (nm)	18.6(2)	17.7(2)	21.2(4)	19.9(4)	20.5(5)
Strain	0.270(5)	0.160(7)	0.060 (12)	0.050 (13)	0.090(13)
*Rwp (%)	5.63	5.48	4.51	4.52	4.80
**Rp (%)	4.31	4.09	3.15	3.29	3.46
***Re (%)	2.65	2.61	2.72	2.87	2.80
****GOF	2.1224	2.1010	1.6557	1.5715	1.7164

* R_{wp}—the weighted profile factor; ** R_p—the profile factor; *** R_e—the expected weighted profile factor; ****GOF—the goodness of fit.

growth in vegetables like lettuce and spinach. In this context, LED lighting that closely aligns with the PAR spectrum and includes additional deep-red components is crucial for future agricultural production.

Trivalent europium – Eu^{3+}—is a lanthanide ion that emits orange, red, and deep red light, corresponding to electronic transitions from its excited $^5D_0$ level to the ground ^7F_J ($J = 1, 2, 3,$ and 4) levels [29]. Owing to the distinctive electronic configuration of trivalent bismuth ions and their tunable luminescent properties, co-doping with Bi^{3+} has the potential to improve the performance of Eu^{3+} activated phosphors. Bi^{3+} ions not only enhance the emission of the primary dopant under UV excitation through their sensitizing and energy transfer capability but may also enable dual-emission and color-tunable photoluminescence [30–35].

In our recent research, we synthesized Sr_2GdF_7 powders with different contents of Eu^{3+} ions (0–100 mol%), demonstrating that continuous exchange of Gd^{3+} with Eu^{3+} does not change the structural type of the compound [36]. Also, it was shown that Eu^{3+} addition causes perpetual emission intensity increase, very high light output, and temperature-stable PL spectra that match the red and far-red absorption spectra of phytochrome plant photoreceptors. Herein, we prepared $Sr_2Gd_{0.2}Eu_{0.8}F_7$ nanopowders doped with different Bi^{3+} contents (0.25, 1, 5, and 10 mol%), for the purpose of determining the influence of Bi^{3+} addition on nanophosphors suitable for horticulture LEDs.

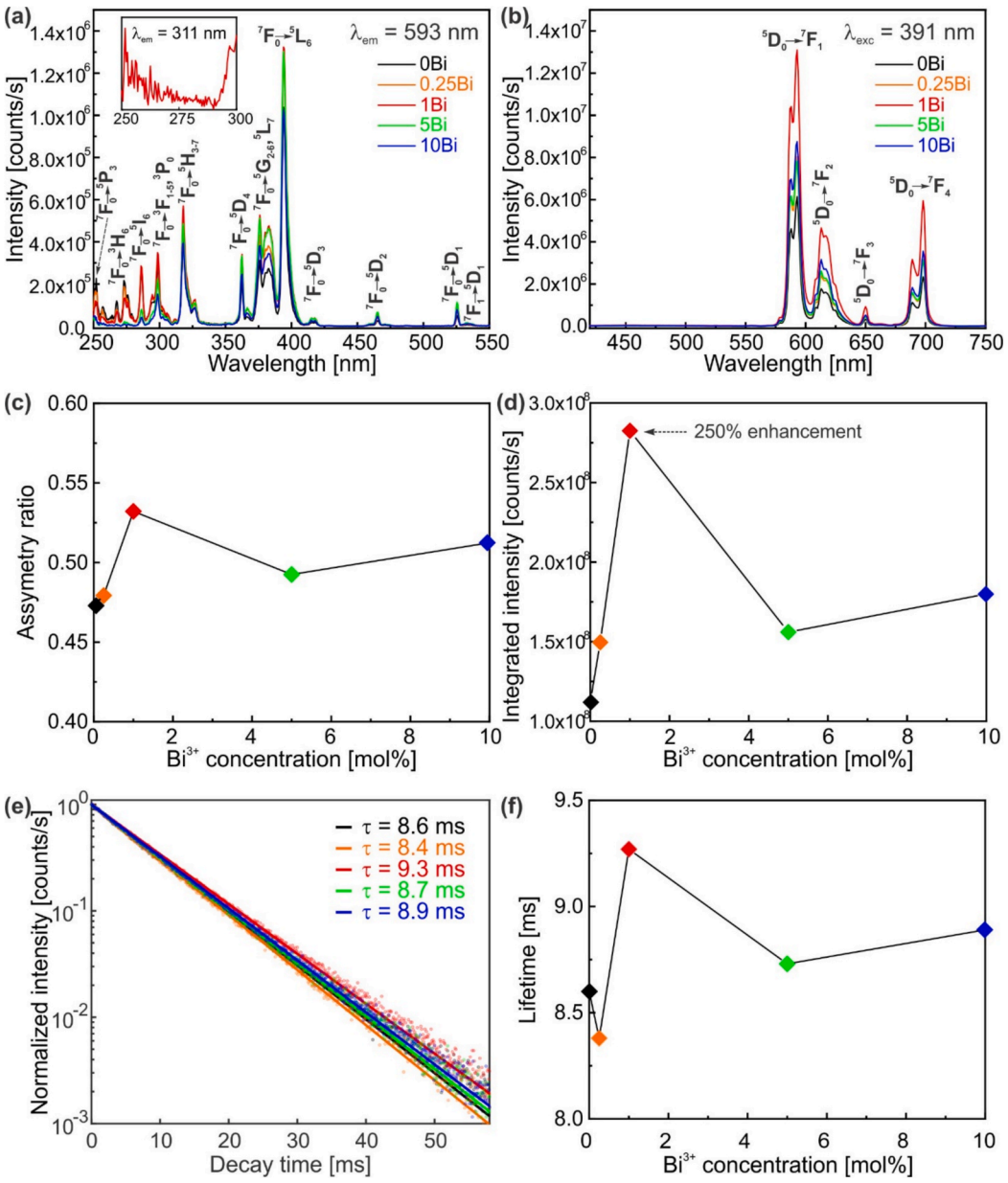

Fig. 2. The photoluminescence of SGEF_xBi, x = 0, 0.25, 1, 5, 10 mol% nanophosphors: (a) excitation spectra under a λ_{em} = 593 nm emission. Inset: excitation spectra under a λ_{em} = 311 nm emission; (b) emission spectra under a λ_{exc} = 391 nm excitation; (c) the asymmetry ratio of $^5D_0 \rightarrow {}^7F_2$ and $^5D_0 \rightarrow {}^7F_1$ transitions versus Bi^{3+} concentration; (d) the integrated emission intensity as a function of Bi^{3+} concentration; (e) the excited state decay curves as a function of Bi^{3+} concentration; (f) the lifetime values depending on the Bi^{3+} content.

Experimental

Materials

Strontium nitrate ($Sr(NO_3)_2$, Thermo Scientific, 99 % min), Gd $(NO_3)_3{\cdot}6H_2O$ (Thermo Scientific, 99.9 %), $Eu(NO_3)_3{\cdot}6H_2O$ (Alfa Aesar, 99.9 %), $Bi(NO_3)_3$ (basic, Kemika, PA), disodium ethylenediaminetetraacetate dihydrate (EDTA-2Na, $C_{10}H_{14}N_2O_8Na_2{\cdot}2H_2O$, Kemika, 99 %) and NH_4F (Alfa Aesar, 98 %), 25 % ammonium solution (NH_4OH, Fisher), nitric acid (65 % HNO_3, Macron fine chemicals), and deionized water were used as starting materials without further purification.

Hydrothermal synthesis

The powders of $Sr_2Gd_{0.2-x}Eu_{0.8}Bi_xF_7$ (x = 0, 0.0025, 0.01, 0.05, 0.10) were prepared using the hydrothermal method. The detailed synthesis description and the procedure scheme were given in [36]. Briefly, bismuth nitrate was dissolved in hot concentrated nitric acid, while the other precursors were dissolved in deionized water. EDTA-2Na was used as a stabilizing agent by forming Sr- and Gd-complexes to prevent particle aggregation during reaction. All precursor solutions were combined, and the pH was adjusted to ~ 6 by adding 25 % ammonium hydroxide solution dropwise. The hydrothermal reaction was conducted in a 100-mL Teflon-lined autoclave at 180 °C for 20 h. After cooling, the precipitates were centrifuged, washed twice with deionized water, and once with a 1:1 ethanol–water mixture to remove any residuals. Finally, the samples were air-dried at 70 °C for 4 h. The Eu^{3+} concentration of 80 mol% was chosen as the one that enables maximal emission intensity in $Sr_2GdF_7{:}Eu^{3+}$ nanophosphors [36]. Therefore, the phosphor host is $Sr_2Gd_{0.2}Eu_{0.8}F_7$, with the abbreviated name SGEF. Table 1 provides the precise quantities of precursors used for the synthesis of 0.0025 mol samples.

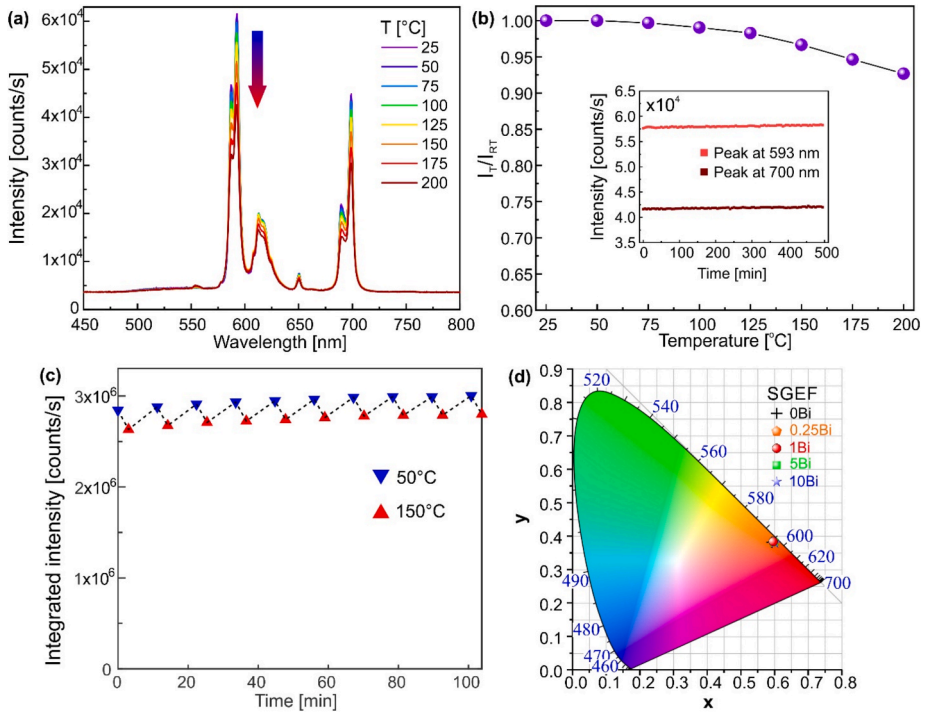

Fig. 3. (a) Temperature-dependent emission spectra of the SGEF_1Bi nanophosphor, in the temperature range 25–200 °C with a 25 °C step; (b) thermal stability of photoluminescence emission of the SGEF_1Bi nanophosphor. The inset shows temporal stability of the two most dominant emission peaks; (c) thermal cycling test of the SGEF_1Bi nanophosphor, performed over 10 repeated cycles between 50 °C and 150 °C; (d) calculated chromaticity coordinates and their position in the CIE color diagram.

Table 3
Colorimetric parameters of SGEF_x Bi, (x = 0, 0.25, 1, 5, 10 mol%) emission.

Bi^{3+} concentration (mol%)	0	0.25	1	5	10
x	0.598	0.601	0.601	0.600	0.602
y	0.388	0.389	0.387	0.389	0.389

Characterization

X-ray diffraction (XRD) analyses were conducted using a Rigaku SmartLab system with Cu Kα radiation at 30 mA and 40 kV to confirm the phase purity and crystallinity of the samples. Diffraction data were collected in the 2θ range of 10° to 90° with a step size of 0.02° and a counting time of 1°/min, while the structural analysis was performed using the integrated PDXL2 package software. A three-dimensional schematic view of the crystal structure is built via the Diamond 4.6.8 software. The powder microstructure was examined using a Mira3 Tescan field emission scanning electron microscope (FE-SEM) operating at an accelerating voltage of 20 kV and the average particle size was calculated using ImageJ software. Diffuse reflectance measurements were performed with the Shimadzu UV-2600 (Shimadzu Corporation, Tokyo, Japan) spectrophotometer equipped with an integrating sphere (ISR-2600), using $BaSO_4$ as the standard reference. Photoluminescence measurements were performed using a Fluorolog-3 Model FL3-221

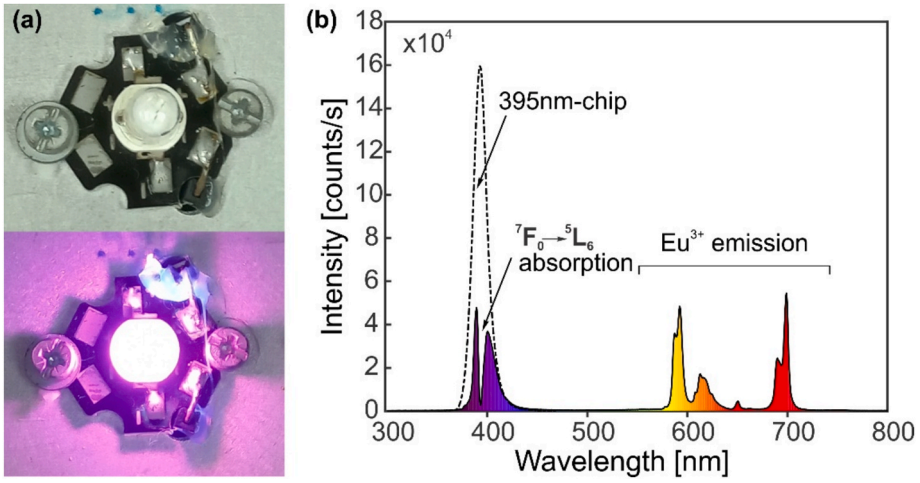

Fig. 4. (a) LED device, fabricated from a SGEF_1Bi nanophosphor with a binder on a 395 nm-emitting semiconductor chip, displaying pinkish violet light; (b) emission spectrum of the as-prepared LED device. The dashed line represents the emission spectrum of a 395 nm chip. The dip at 391 nm corresponds to the $^7F_0 \rightarrow {}^5L_6$ absorption transition of Eu^{3+}. (For interpretation of the references to color in this figure legend, the reader is referred to the web version of this article.)

spectrofluorometer system (Horiba JobinYvon), equipped with a 450 W Xenon lamp and TBX detector for steady-state emission measurements, while for emission decay measurements, a xenon–mercury pulsed lamp was utilized. The excitation spectra were recorded at the emission wavelength of 593 nm, with a long-pass 550 nm filter mounted in front of the detector, whereas the emission spectra were observed upon a 391 nm excitation. Quantum efficiency measurements were carried out using a custom-built setup consisting of an Ocean Insight IDP-REF 38.1 mm integrating sphere, fiber-coupled to an Ocean Insight LSM-405A LED light source at the reference port and an OCEAN-FX-XR1-ES extended-range spectrometer at the sample port of the sphere, with $BaSO_4$ employed as the standard reference. Thermal stability of the photoluminescent emission within the temperature range of 25–200 °C was estimated using the OceanOptics spectrofluorometric system upon a 365 nm excitation (OceanOptics LED, L365A), coupled with a Micro-Optik heating stage. The thermal cycling test was carried out through 10 consecutive cycles of heating and natural cooling in the temperature range of 50 °C to 150 °C. A 395 nm LED chip with 100 mW optical power was used to excite a mixture of luminescent powder with transparent high-temperature inorganic binder (Cerambind 643–2 from Aremco). The emission spectrum of as-prepared LED device was recorded with the OceanOptics spectrofluorometric system.

Results and discussion

Structure and morphology analysis

The XRD patterns of the synthesized SGEF_*x*Bi ($x = 0$, 0.25, 1, 5, 10 mol%) nanophosphors are displayed in Fig. 1(a), together with the corresponding ICDD 01–083-3680 data. It was already proved that both Sr_2GdF_7 and Sr_2EuF_7 crystallize in the form of cubic $Fm\,\bar{3}\,m$ structure [36]. In consistence with this, all SGEF_*x*Bi samples are single-phased with the cubic structure and $Fm\,\bar{3}\,m$ symmetry group. Inside this structural type, presented schematically in three-dimensional view in Fig. 1(b), Sr^{2+} and Gd^{3+} ions both occupy Wyckoff site 4a with m-3 m symmetry, and F^- ions reside in Wyckoff site 8c with − 43 m symmetry. In an ideal fluorite-type MX_2 compound, cations fill 8-coordinate cubic sites, and anions occupy 4-coordinate tetrahedral sites. Nevertheless, in Sr_2GdF_7, the partial occupancy of both cation and anion sites leads to deviations from these ideal geometries, resulting in a variety of local coordination environments for the constituent species [36]. When it comes to the structural type of Sr_2GdF_7 and related compounds, there is a discrepancy between data in different literature reports. Some articles report on cubic $Fm\,\bar{3}\,m$ structure [22,37,38] and others have a tetragonal structure [19,20,39–41]. However, in several articles that claim the tetragonal structure of Sr_2GdF_7, the XRD data lack the expected tetragonal superstructure peaks and instead match a cubic structure – consistent with the materials studied here. We can assume that further high-temperature annealing of these hydrothermally synthesized samples may induce a transition from the disordered cubic fluorite-type structure to an ordered tetragonal phase. The ionic radii of Gd^{3+} (Gd^{3+}_{VIII} = 1.053Å), Eu^{3+} (Eu^{3+}_{VIII} = 1.066Å) and Bi^{3+} (Bi^{3+}_{VIII} = 1.17Å) [42] are comparable, and they have the same oxidation state. Although Bi^{3+} ions could theoretically substitute either Gd^{3+} or Eu^{3+} ions, the systematic decrease in Gd^{3+} content with increasing Bi^{3+} concentration (refer to Table 1) indicates a preferential substitution of Gd^{3+} by Bi^{3+} in the SGEF host lattice. This is also supported by the fact that no additional phases with Eu^{3+} were detected. The structural parameters of the SGEF_*x*Bi nanophosphors, determined using the built-in PDXL2 package software, are presented in Table 2. The unit cell parameter and crystallite size (~20 nm) do not change significantly with the Bi^{3+} co-doping, compared to the SGEF sample.

The scanning electron microscopy image of the representative SGEF_1Bi sample in Fig. 1(c) The microstructure observed at 100 k × magnification reveals agglomerated nanoparticles with quasi-spherical morphologies. The particles form porous, loosely packed clusters, typical for fluoride-based nanophosphors synthesized via wet-chemical routes [33]. The particle size was estimated by measuring the diameter of more than 100 particles and fitting the histogram in Fig. 1(d) using a lognormal distribution. The particles exhibit a size distribution in 30–100 nm range. The average particle size was calculated to be 51 ± 4 nm. This value is higher than the crystallite size obtained from the XRD data, suggesting that each particle consists of several crystallites.

Photoluminescence spectra and decay times

The photoluminescence excitation spectra of the SGEF_*x*Bi ($x = 0$, 0.25, 1, 5, 10 mol%) samples, recorded at the fixed emission wavelength of 593 nm, are presented in Fig. 2(a). All the peaks correspond to the intra-*4f* electronic transitions of the Eu^{3+} ion and are assigned according to literature [22,36,43,44]. In contrast to previously reported data [36], characteristic gadolinium peaks at 273 nm and 311 nm were not detected in the excitation spectra. Although the Eu^{3+} transition at 273 nm, noted as $^7F_0 \rightarrow {}^3H_6$ in Fig. 2(a), coincides with the $^8S_{7/2} \rightarrow {}^6I_J$ transition of Gd^{3+}, its absence was proved by recording the excitation spectra under a 311 nm-emission (shown in Fig. 2(a), inset). This means there is no energy transfer from Gd^{3+} to Eu^{3+} ions, probably due to the prevalence of Eu^{3+} ions in the SGEF host. The addition of Bi^{3+} as a co-dopant causes a moderate increase in excitation intensity of Eu^{3+} transitions.

The samples' emission spectra upon a 391 nm-excitation (Fig. 2(b)) expose the typical *4f* – *4f* transitions of Eu^{3+}, located around 593 nm ($^5D_0 \rightarrow {}^7F_1$), 613 nm ($^5D_0 \rightarrow {}^7F_2$), 650 nm ($^5D_0 \rightarrow {}^7F_3$), 698 nm ($^5D_0 \rightarrow {}^7F_4$ transition) [29,44]. The $^5D_0 \rightarrow {}^7F_1$ transition in Eu^{3+} is a magnetic-dipole transition that is insensitive to the surrounding environment. In contrast, the $^5D_0 \rightarrow {}^7F_2$ transition is a forced electric-dipole transition known for its hypersensitivity to changes in the local environment around the Eu^{3+} ions. The emission spectra of all the samples exhibit the atypically intense $^5D_0 \rightarrow {}^7F_4$ emission peak around 700 nm, adding a favorable spectral window that coincides with the deep-red part of the PAR spectrum [24].

The emission from the $^5D_0 \rightarrow {}^7F_1$ transition dominates the emission spectrum when Eu^{3+} ions are situated in crystallographic sites with high symmetry. Our experimental findings are consistent with these predictions, as the $^5D_0 \rightarrow {}^7F_1$ transition exhibits the utmost intensity, and the XRD patterns indicate the structure of high symmetry. A valuable indicator of the variations in local symmetry surrounding the Eu^{3+} ion is the asymmetry ratio, *R*. It is defined as the ratio of intensities of the $^5D_0 \rightarrow {}^7F_2$ and $^5D_0 \rightarrow {}^7F_1$ transitions, by a following equation: [45]:

$$R = \frac{I(^5D_0 \rightarrow {}^7F_2)}{I(^5D_0 \rightarrow {}^7F_1)} \quad (1)$$

Asymmetry ratio values below 1 indicate that the magnetic dipole transition dominates the emission spectra [45]. As shown in Fig. 2(c) the asymmetry ratio exhibits a change with the Bi^{3+} content increase, suggesting that the local symmetry of the emitting ion is slightly altered. The highest asymmetry ratio is observed for the SGEF_1Bi sample.

Fig. 2(d) unveils that Bi^{3+} co-doping of the SGEF nanophosphor causes emission intensity increase for all examined concentrations, while for the SGEF_1Bi sample, the integral emission intensity enhances by 250 %, compared to the Bi-free sample.

To investigate the energy transfer from Bi^{3+} to Eu^{3+}, the diffuse reflectance spectrum, the photoluminescence emission spectra under a 265 nm excitation, along with the corresponding explanation, are provided in the Supplementary Information (Fig. S1).

Fig. 2(e) demonstrates the normalized photoluminescence lifetime decay curves of SGEF nanophosphors with varying bismuth concentrations, measured at room temperature. The decay profiles were analyzed by fitting the experimental data to a simple single-exponential function to determine the corresponding lifetime (τ) values [46].

$$I(t) = I_0 e^{-\frac{t}{\tau}} \quad (2)$$

where $I(t)$ represents the corresponding emission intensity at time t, I_0 represents the corresponding emission intensity at time $t = 0$ (ideally $I_0 = 1$ for normalized $I(t)$), and τ is the emission decay constant (the excited state lifetime). All the excited $^5D_0$ state lifetimes are quite long and alter with the Bi^{3+} content, resembling the emission intensity change (see Fig. 2(f)). The optimized SGEF_1Bi sample exhibits a lifetime value of 9.3 ms.

Similar trends in Figs. 2(c), (d) and (f) indicate that Bi^{3+} co-doping causes the lattice distortion that further leads to the breaking of the partially forbidden transitions of Eu^{3+} ions and enhances photoluminescent properties [47]. Generally, when the Bi^{3+} content increases, both the emission intensity and lifetime decrease. This decline may also be attributed to the formation of Bi^{3+} ion clusters at higher doping levels, which introduce numerous defect states within the crystal lattice and promote nonradiative recombination pathways [48]. In our study, the integrated emission intensity and lifetime at $x = 10$ are higher than at $x = 5$ mol% (see Figs. 2(b), (d), (f)). While the 2 % increase in lifetime falls within the range of experimental error, the integrated intensity shows a more pronounced increase of about 13 %. This indicates that lattice distortion, along with the relaxation of forbidden Eu^{3+} transitions, is the principal factor underlying the unusually enhanced emission intensity observed in the 5–10 mol% Bi^{3+} concentration range.

As reported previously, the $Sr_2Gd_{0.2}Eu_{0.8}F_7$ phosphor (Sr_2GdF_7:80 mol% Eu^{3+}) exhibits a quantum efficiency of 60.4 % [36]. In comparison, the Bi^{3+}-doped counterpart ($Sr_2Gd_{0.2}Eu_{0.8}F_7$:1 mol% Bi) achieves a higher quantum efficiency of 67.2 %, clearly demonstrating the positive influence of Bi^{3+} incorporation on the luminescent performance.

Thermal stability and LED fabrication of the optimized SGEF_1Bi nanophosphor

For horticulture LED applications, the appropriate color of the light source and the thermal stability of the photoluminescence emission are important requirements. According to some LED manufacturers, 100 °C is typically regarded as the maximum operating temperature for LEDs [49–51], even though temperature stability up to 150 °C is often reported in the literature [52–54]. To evaluate the thermal stability of the photoluminescence emission, steady-state temperature-dependent photoluminescence measurements were conducted over the 25–200 °C range with a 25 °C step using the SGEF_1Bi sample pressed into a pellet. The resulting spectra, displayed in Fig. 3 (a), reveal a minor decrease of overall emission intensity. From these spectra, thermal stability of the optimized sample is derived and shown in Fig. 3(b). It is evident that SGEF_1Bi demonstrates outstanding thermal stability, retaining 99 % of its room-temperature integrated emission intensity at 100 °C and maintaining 93 % of its initial emission even at a temperature of 200 °C. The inset in Fig. 3(b) displays good temporal stability of the two most dominant emission peaks – at 593 nm ($^5D_0 \rightarrow {}^7F_1$ transition) and 700 nm ($^5D_0 \rightarrow {}^7F_4$ transition), extracted from spectra recorded every 5 min, during 500 min. Thermal cycling test of the SGEF_1Bi nanophosphor, displayed in Fig. 3(c), proves the thermal stability is preserved even after 10 consecutive heating–cooling cycles.

To evaluate the color of the synthesized nanophosphors, CIE (Commission Internationale de l'Éclairage) chromaticity coordinates were derived from the photoluminescence emission spectra. They provide a standard method for representing and describing colors, and the color is typically plotted using the (x, y) coordinates on the CIE 1931 chromaticity diagram. The CIE chromaticity coordinates, calculated from the samples' emission spectra are shown in Fig. 3(d) and Table 3. The results reveal that the coordinates remain nearly the same across all compositions, consistently falling within the orange–red region of the chromaticity diagram, thereby ensuring stable emission color.

Finally, the powder sample with the highest emission intensity, SGEF_1Bi, was mixed with a ceramic binder and pressed onto a 395 nm near-UV LED chip to authenticate the application potential of these phosphors in LEDs. Photographs of the fabricated LED device, shown in Fig. 4(a), display strong pinkish violet light emission when the power supply is on. The emission spectrum of this LED system is presented in Fig. 4(b). The characteristic europium emission transitions in the red and deep-red spectral range are clearly visible. Dashed line in Fig. 4(b). represents the emission spectrum of a 395 nm chip. Two peaks around 400 nm are the result of the chip's emission and europium's absorption transition of $^7F_0 \rightarrow {}^5L_6$ at 391 nm (refer to excitation spectrum in Fig. 2 (a)). Eu^{3+} strongly absorbs energy from the chip's emission peak, resulting in a doublet near 400 nm.

Conclusion

This study reports the synthesis of $Sr_2Gd_{0.2}Eu_{0.8}F_7$ nanoparticles doped with varying concentrations of Bi^{3+} by the hydrothermal method. The excitation spectra of SGEF_*x*Bi nanophosphors (λ_{em} = 593 nm) exhibit characteristic intra-*4f* electronic transitions of the Eu^{3+} ions. The emission spectra upon 391 nm excitation unveil orange/red and deep-red emission of Eu^{3+}, with the most dominant $^5D_0 \rightarrow {}^7F_1$ transition (as expected for the cubic structure), and the atypically intense $^5D_0 \rightarrow {}^7F_4$ transition. The addition of Bi^{3+} ions in different concentrations in SGEF phosphors induces enhancement of Eu^{3+} emission, with 1 mol% being the optimal concentration. For the optimized sample, the integrated emission intensity amplifies by a stunning 250 %, while further addition of Bi^{3+} (up to 10 mol%) leads to the improvement of 60 %. The calculated asymmetry ratio changes moderately with Bi^{3+} content, indicating a disturbance in the local symmetry around the emitting Eu^{3+} ions. The luminescence lifetime exhibits a similar dependence on Bi^{3+} concentration. However, above 1 mol% Bi^{3+} doping, emission intensities and lifetime values decrease due to concentration quenching and Bi^{3+} clustering, which introduces defects and promotes nonradiative recombination. The calculated CIE coordinates are in the red portion of the color diagram, while the thermal stability of emission is exceptional – 99 % of the room-temperature emission is maintained at 100 °C and 93 % at a temperature of 200 °C. These findings prove that Bi^{3+} activated $Sr_2Gd_{0.2}Eu_{0.8}F_7$ nanophosphors provide favorable spectral features, suitable for LED applications in horticulture. Upcoming research efforts will focus on evaluation of the impact of these nanophosphors on plant growth in relevant environment.

CRediT authorship contribution statement

Lj. Đačanin Far: Writing – original draft, Visualization, Project administration, Investigation, Data curation. **J. Periša:** Investigation. **I. Zeković:** Investigation. **Z. Ristić:** Investigation, Formal analysis. **M. Medić:** Investigation. **M.D. Dramićanin:** Writing – review & editing, Supervision, Conceptualization. **B. Milićević:** Writing – review & editing, Supervision, Project administration, Funding acquisition, Conceptualization.

Declaration of competing interest

The authors declare the following financial interests/personal relationships which may be considered as potential competing interests: Ljubica Dacanin Far reports financial support was provided by Science Fund of the Republic of Serbia. If there are other authors, they declare that they have no known competing financial interests or personal relationships that could have appeared to influence the work reported in this paper.

Acknowledgement

This research was supported by the Science Fund of the Republic of Serbia, #GRANT No 10412, LED technology based on bismuth-

sensitized Eu^{3+} luminescence for cost-effective indoor plant growth - LEDTech-GROW (Authors: Lj. Đačanin Far, J. Periša, B. Milićević). All authors acknowledge funding from the Ministry of Science, Technological Development, and Innovation of the Republic of Serbia under contract 451-03-136/2025-03/ 200017.

Appendix A. Supplementary data

Supplementary data to this article can be found online at https://doi.org/10.1016/j.rinp.2025.108495.

Data availability

Data will be made available on request.

References

[1] Pawade VB, Pawar NR, Dhoble SJ. Upconversion in some fluoride crystal system –a review. Infrared Phys Technol 2022;123:104148. https://doi.org/10.1016/j.infrared.2022.104148.
[2] Krämer KW, Biner D, Frei G, Güdel HU, Hehlen MP, Lüthi SR. Hexagonal sodium yttrium fluoride based green and blue emitting upconversion phosphors. Chem Mater 2004;16:1244–51. https://doi.org/10.1021/cm031124o.
[3] Runowski M, Bartkowiak A, Majewska M, Martín IR, Lis S. Upconverting lanthanide doped fluoride $NaLuF_4$:Yb^{3+}-Er^{3+}-Ho^{3+} - optical sensor for multi-range fluorescence intensity ratio (FIR) thermometry in visible and NIR regions. J Lumin 2018;201:104–9. https://doi.org/10.1016/j.jlumin.2018.04.040.
[4] Molina-González J, Rivera AA, Ramírez-García G. A solvothermal method for the synthesis of dual paramagnetic and upconverting luminescent β-$NaYF_4$:Yb^{3+},Ln^{3+}@$NaGdF_4$ (Ln^{3+}=Er^{3+} or Tm^{3+}) core@shell nanoparticles. Ceram Int 2024;50:44339–46. https://doi.org/10.1016/j.ceramint.2024.08.282.
[5] Nosov VG, Betina AA, Bulatova TS, Guseva PB, Kolesnikov IE, Orlov SN, et al. Effect of Gd^{3+}, La^{3+}, Lu^{3+} co-doping on the morphology and luminescent properties of $nayf_4$:sm^{3+} phosphors. Materials 2023;16:2157. https://doi.org/10.3390/ma16062157.
[6] Prichisly KS, Betina AA, Petrova AL, Bulatova TS, Orlov SN, Kolesnikov IE, et al. Synthesis, morphology, and luminescent properties of nanocrystalline KYF_4:Eu^{3+} phosphors. Crystals (Basel) 2025;15:500. https://doi.org/10.3390/cryst15060500.
[7] Cheng H, Li T, Guo L, Zhang K, Zhu C. Tunable photoluminescence of Ba_2GdF_7: Tb^{3+}, Eu^{3+} nanoparticles based on energy transfer. J Lumin 2023;261:119914. https://doi.org/10.1016/j.jlumin.2023.119914.
[8] Feng Y, Chen H, Shao B, Zhao S, Wang Z, You H. Renal-clearable peptide-functionalized Ba_2GdF_7 nanoparticles for positive tumor-targeting dual-mode bioimaging. ACS Appl Mater Interfaces 2018;10:25511–8. https://doi.org/10.1021/acsami.8b07129.
[9] Wang W, Wei X, Chen H, Pan Y, Li Y. Tunable up-conversion in glass–ceramics containing Ba_2YF_7: Ho^{3+}/Yb^{3+} nanocrystals via Ce3+ doping. Appl Phys A 2022;128:304. https://doi.org/10.1007/s00339-022-05424-0.
[10] Li H, Zhao Y, Kolesnikov I, Xu S, Chen L, Bai G. Multifunctional rare earth ions-doped Ba_2LaF_7 nanocrystals for simultaneous temperature sensing and photothermal therapy. J Alloy Compd 2023;931:167535. https://doi.org/10.1016/j.jallcom.2022.167535.
[11] Tan Y, Wang H, Xiang L, Zhou H, Kong L, Zhang H, et al. A water-soluble and upconverting Sr_2LaF_7: Yb/Er@PSIoAm bio-probe for in vitro/vivo fluorescence imaging. Opt Mater (Amst) 2021;111:110652. https://doi.org/10.1016/j.optmat.2020.110652.
[12] Yan M, Liu Y, Pei X, Fan L, Liu L, Li C, et al. A novel Gd^{3+}-doping-induced enhancement of Sr_2YF_7: Dy^{3+} phosphor photoluminescence and thermal stability for white light-emitting diodes. J Alloy Compd 2025;1020:179509. https://doi.org/10.1016/j.jallcom.2025.179509.
[13] Guo MY, Shen LF, Pun EYB, Lin H. Sr_2GdF_7: Er^{3+}/Yb^{3+} nanocrystal-inlaid pliable fibers for synergistic feedback temperature monitoring. J Lumin 2022;252:119394. https://doi.org/10.1016/j.jlumin.2022.119394.
[14] Runowski M, Goderski S, Przybylska D, Grzyb T, Lis S, Martín IR. Sr2LuF7:Yb3+–Ho3+–Er3+ upconverting nanoparticles as luminescent thermometers in the first, second, and third biological windows. ACS Appl Nano Mater 2020;3:6406–15. https://doi.org/10.1021/acsanm.0c00839.
[15] Il PY, Kim JH, Lee KT, Jeon K, Bin NH, Yu JH, et al. Nonblinking and nonbleaching upconverting nanoparticles as an optical imaging nanoprobe and T1 magnetic resonance imaging contrast agent. Adv Mater 2009;21:4467–71. https://doi.org/10.1002/adma.200901356.
[16] Xiang L, Wang C, Mao Y, Jiang Y, Hu Z, Wang Y. Construction of a multifunctional bio-probe based on lanthanides for UCL/MR/CT multimodal imaging in vivo. Biomed Mater 2025;20:025005. https://doi.org/10.1088/1748-605X/ada3d0.
[17] Xiang L, Ren G, Mao Y, He J, Su R. Controllable synthesis and upconversion emission of ultrasmall lanthanide-doped Sr_2GdF_7 nanocrystals. Opt Mater (Amst) 2015;49:6–14. https://doi.org/10.1016/j.optmat.2015.08.014.
[18] Chen C, Liu J, Chen Y, Li C, Liu X, Huang H, et al. Sub-10 nm Sr_2LuF_7:Yb/Er@Sr_2GdF_7@SrF_2 up-conversion nanocrystals for up-conversion luminescence–magnetic resonance–computed tomography trimodal bioimaging. ACS Appl Mater Interfaces 2017;9:5748–56. https://doi.org/10.1021/acsami.6b14007.
[19] Chen W, Cao J, Hu F, Wei R, Chen L, Guo H. Sr_2GdF_7:Tm^{3+}/Yb^{3+} glass ceramic: a highly sensitive optical thermometer based on FIR technique. J Alloy Compd 2018;735:2544–50. https://doi.org/10.1016/j.jallcom.2017.11.201.
[20] Hu F, Zhang J, Giraldo O, Song W, Wei R, Yin M, et al. Spectral conversion from green to red in Yb^{3+}/Ho^{3+}:Sr_2GdF_7 glass ceramics via Ce^{3+} doping. J Lumin 2018;201:493–9. https://doi.org/10.1016/j.jlumin.2018.05.007.
[21] Pan Y, Wei X, Wang W, Chen H, Li Y. Monodispersed Sr_2GdF_7:Yb^{3+}, Er^{3+} nanocrystals: hydrothermal synthesis and optical temperature sensing behavior. Opt Mater (Amst) 2020;107:110156. https://doi.org/10.1016/j.optmat.2020.110156.
[22] Runowski M, Balabhadra S, Lis S. Nanosized complex fluorides based on Eu^{3+} doped Sr_2LnF_7 (Ln=La, Gd). J Rare Earths 2014;32:242–7. https://doi.org/10.1016/S1002-0721(14)60058-2.
[23] Zhen S, Bugbee B. Far-red photons have equivalent efficiency to traditional photosynthetic photons: implications for redefining photosynthetically active radiation. Plant Cell Environ 2020;43:1259–72. https://doi.org/10.1111/pce.13730.
[24] Li H, Niu Y, Liu C, Jiang H, Li J, Wu J, et al. Unraveling the remarkable influence of square antiprism geometry on highly efficient far-red emission of Eu^{3+} in borotellurate phosphors for versatile utilizations. Laser Photon Rev 2024;18. https://doi.org/10.1002/lpor.202400843.
[25] Huang C, Chen Y, Wu F, Zhang Q, Teng Y, Zhang X, et al. Broadband far-red/near-infrared emission of Fe^{3+} and Mn^{4+} co-doped $MgAl_2O_4$ phosphors for plant lighting. Mater Chem Front 2025;9:2879–88. https://doi.org/10.1039/D5QM00548E.
[26] Elias E, Brache K, Schäfers J, Croce R. Coloring outside the lines: exploiting pigment–protein synergy for far-red absorption in plant light-harvesting complexes. J Am Chem Soc 2024;146:3508–20. https://doi.org/10.1021/jacs.3c13373.
[27] Dou H, Li X, Li Z, Song J, Yang Y, Yan Z. Supplementary far-red light for photosynthetic active radiation differentially influences the photochemical efficiency and biomass accumulation in greenhouse-grown lettuce. Plants 2024;13:2169. https://doi.org/10.3390/plants13152169.
[28] Wang Y, Oliver TJ, Croce R, Long SP. Addition of longer wavelength absorbing chlorophylls into crops could increase their photosynthetic productivity by 26%. Nat Commun 2025;16:7933. https://doi.org/10.1038/s41467-025-62885-6.
[29] Serna-Gallén P, Beltrán-Mir H, Cordoncillo E. Practical guidance for easily interpreting the emission and physicochemical parameters of Eu^{3+} in solid-state hosts. Ceram Int 2023;49:41078–89. https://doi.org/10.1016/j.ceramint.2023.01.141.
[30] Xu D, Yu P, Tian L. Luminescence properties of Pr^{3+} and Bi^{3+} co-doped $NaCaTiNbO_6$ phosphor for red-LEDs. J Rare Earths 2018;36:243–7. https://doi.org/10.1016/j.jre.2017.07.013.
[31] Wei R, Guo J, Li K, Yang L, Tian X, Li X, et al. Dual-emitting SrY_2O_4:Bi^{3+},Eu^{3+} phosphor for ratiometric temperature sensing. J Lumin 2019;216:116737. https://doi.org/10.1016/j.jlumin.2019.116737.
[32] Zhang M, Jia M, Sheng T, Fu Z. Multifunctional optical thermometry based on the transition metal ions doped down-conversion Gd_2ZnTiO_6:Bi^{3+},Mn^{4+} phosphors. J Lumin 2021;229:117653. https://doi.org/10.1016/j.jlumin.2020.117653.
[33] Milenković K, Đačanin Far L, Kuzman S, Antić Ž, Ćirić A, Dramićanin MD, et al. Red emission enhancement in $BaYF_5$:Eu^{3+} phosphor nanoparticles by Bi^{3+} co-doping. Opt Express 2024;32:41632. https://doi.org/10.1364/OE.542685.
[34] Cao R, Liang R, Li L, Liu R, Chen T, Lan B, et al. Luminescence properties, tunable emission and energy transfer of $Ca_9MgLi(PO_4)_7$:Bi^{3+}/Eu^{3+} phosphor. J Lumin 2022;252:119397. https://doi.org/10.1016/j.jlumin.2022.119397.
[35] Huang Z, Wu F, Zhang Q, Teng Y, Mu Z. High sensitivity temperature sensing material $In_2Li_3P_3O_{12}$:Bi^{3+},Eu^{3+} based on effective energy transfer from Bi^{3+} to Eu^{3+}. Ceram Int 2024;50:32180–6. https://doi.org/10.1016/j.ceramint.2024.06.025.
[36] Milićević B, Ćirić A, Ristić Z, Medić M, Alodhayb AN, Evans IR, et al. Eu^{3+}-activated Sr_2GdF_7 colloid and nano-powder for horticulture LED applications. J Alloy Compd 2025;1010:177820. https://doi.org/10.1016/j.jallcom.2024.177820.
[37] Grzyb T, Przybylska D. Formation mechanism, structural, and upconversion properties of alkaline rare-earth fluoride nanocrystals doped with Yb^{3+}/Er^{3+} Ions. Inorg Chem 2018;57:6410–20. https://doi.org/10.1021/acs.inorgchem.8b00484.
[38] Sorokin NI, Karimov DN, Sul'yanova EA, Sobolev BP. Nanostructured crystals of fluorite phases $Sr_{1-x}R_xF_{2+x}$ and their ordering: 12. Influence of structural ordering on the fluorine-ion conductivity of $Sr_{0.667}R_{0.333}F_{2.333}$ alloys (R = Tb or Tm) at their annealing. Crystallogr Rep 2018;63:121–6. https://doi.org/10.1134/S1063774518010182.
[39] Teng L, Zhang W, Chen W, Cao J, Sun X, Guo H. Highly efficient luminescence in bulk transparent Sr_2GdF_7:Tb^{3+} glass ceramic for potential X-ray detection. Ceram Int 2020;46:10718–22. https://doi.org/10.1016/j.ceramint.2020.01.079.
[40] Xia Z, Du P, Liao L. Facile hydrothermal synthesis and upconversion luminescence of tetragonal Sr_2LnF_7:Yb^{3+}/Er^{3+}(Ln = Y, Gd) nanocrystals. Physica Status Solidi (A) 2013;210:1734–7. https://doi.org/10.1002/pssa.201329114.
[41] Sarkar S, Graña-Suárez L, Verboom W, Mahalingam V, Huskens J. A luminescent nanocrystal marker for the selective and ultrasensitive detection of explosives. ChemNanoMat 2016;2:805–9. https://doi.org/10.1002/cnma.201600184.
[42] Shannon RD. Revised effective ionic radii and systematic studies of interatomic distances in halides and chalcogenides. Acta Crystallographica Section A 1976;32:751–67. https://doi.org/10.1107/S0567739476001551.

[43] Đačanin Far L, Ćirić A, Ristić Z, Periša J, Dramićanin T, Lukić-Petrović SR, et al. Photoluminescence of $Y_3NbO_7:Eu^{3+}$ powders. Ceram Int 2022;48:28250–7. https://doi.org/10.1016/j.ceramint.2022.06.130.
[44] Niu Y, Wu F, Zhuo Y, Li J, Zhang Q, Teng Y, et al. Luminescence properties and applications of Ca_2ScTaO_6: Bi^{3+},Ln^{3+}(Ln = Eu, Sm, Dy, Tb) phosphors. Ceram Int 2025;51:30597–603. https://doi.org/10.1016/j.ceramint.2025.04.252.
[45] Kolesnikov IE, Povolotskiy AV, Mamonova DV, Kolesnikov EY, Kurochkin AV, Lähderanta E, et al. Asymmetry ratio as a parameter of Eu^{3+} local environment in phosphors. J Rare Earths 2018;36:474–81. https://doi.org/10.1016/j.jre.2017.11.008.
[46] Brik MG, Slidos I, Kiisk V. Introduction to spectroscopy of atoms. Molecules and Crystals. Tartu University Press; 2008.
[47] Ding Y, Li Z. Tuning the photoluminescence properties of β-$NaYF_4$:Yb,Er by Bi^{3+} doping strategy. Cryst Res Technol 2022;57. https://doi.org/10.1002/crat.202100162.
[48] Pang X, Zhang Y, Ding L, Su Z, Zhang WF. Upconversion luminescence properties of Er^{3+}–Bi^{3+} codoped $CaSnO_3$ nanocrystals with perovskite structure. J Nanosci Nanotechnol 2010;10:1860–4. https://doi.org/10.1166/jnn.2010.2135.
[49] https://downloads.cree-led.com/files/fs/XLamp-Discrete-Directional-Feature-Sheet.pdf n.d.
[50] https://ams-osram.com/products/leds/color-leds/osram-chip-led-0402-lb-qh9g n.d.
[51] Zhuo Y, Niu Y, Wu F, Li J, Wang Y, Zhang Q, et al. Super-wide-range tunable emission across NIR-II and NIR-III achieved by B-site cation co-substitution in Ni^{2+}-doped double perovskites for NIR light sources. J Mater Chem C Mater 2025;13:10621–31. https://doi.org/10.1039/D5TC00613A.
[52] Liu Y, Zhang J, Zhang C, Xu J, Liu G, Jiang J, et al. $Ba_9Lu_2Si_6O_{24}:Ce^{3+}$: an efficient green phosphor with high thermal and radiation stability for solid-state lighting. Adv Opt Mater 2015;3:1096–101. https://doi.org/10.1002/adom.201500078.
[53] Yang C, Liu W, You Q, Zhao X, Liu S, Xue L, et al. Recent advances in light-conversion phosphors for plant growth and strategies for the modulation of photoluminescence properties. Nanomaterials 2023;13:1715. https://doi.org/10.3390/nano13111715.
[54] Cao R, Bai J, Nie J, Cheng F, Lan B, Zhang L, et al. Broadband NIR emission properties of Fe^{3+}-activated aluminate with double peaks via occupying two sites. J Alloy Compd 2025;1021:179639. https://doi.org/10.1016/j.jallcom.2025.179639.